Model for the conversion of nuclear waste melter feed to glass

Richard Pokorny[a], Pavel Hrma[b,c]

[a]Department of Chemical Engineering, Institute of Chemical Technology in Prague, Technicka 5, 166 28 Prague 6, Czech Republic

[b]Pacific Northwest National Laboratory, 902 Battelle Blvd., Richland WA 99352 USA

[c]Division of Advanced Nuclear Engineering, Pohang University of Science and Technology, Pohang, Republic of Korea

Abstract

The rate of batch-to-glass conversion is a primary concern for the vitrification of nuclear waste, as it directly influences the life cycle of the cleanup process. This study describes the development of an advanced model of the cold cap, which augments the previous model by further developments on the structure and the dynamics of the foam layer. The foam layer on the bottom of the cold cap consists of the primary foam, cavities, and the secondary foam, and forms an interface through which the heat is transferred to the cold cap. Other model enhancements include the behavior of intermediate crystalline phases and the dissolution of quartz particles. The model relates the melting rate to feed properties and melter conditions, such as the molten glass temperature, foaminess of the melt, or the heat fraction supplied to the cold cap from the plenum space. The model correctly predicts a 25% increase in melting rate when changing the alumina source in the melter feed from $Al(OH)_3$ to AlO(OH). It is expected that this model will be incorporated in the full glass melter model as its integral component.

Keywords

glass melting, glass foaming, waste vitrification, cold cap

1. Introduction

In an all-electric glass melter, the glass batch, or the melter feed, is charged on the top of the molten glass, where it forms a floating layer of reacting and melting feed material, the cold cap. The cold cap, also called a batch blanket, is only several centimeters thick, yet the temperature difference between its top and bottom can be as high as 1000 K and the entire conversion process of the melter feed to molten glass is nearly completed within it. The cold cap structure established during steady-state melting is largely affected by the melter feed makeup, and through its effect on the rate of melting has a decisive impact on the production efficiency. For example, the increased melting rate can significantly shorten the life cycle of the cleanup process at the Hanford Site in Washington State, USA, where more than 200,000 m^3 of nuclear waste will be vitrified over the next decades [1].

In spite of its importance, mathematical models of glass-melting furnaces, even those most recent [2,3,4], rarely model the batch conversion process. Instead, they assume a uniform inlet velocity with a prescribed temperature at the batch-melt interface. Only a few researchers (Mase and Oda [5], Viskanta and Wu [6], Ungan and Viskanta [7], Hrma [8], and Schill [9,10]) developed simplified one-dimensional (1D) or two-dimensional models for the batch charged into gas-heated furnaces.

During the final stages of the feed-to-glass conversion process in the cold cap, reaction gases produce primary foam. Also, oxygen bubbles from redox reactions within the melt produce secondary foam. Foam impacts the heat transfer from the underlying melt and becomes a dominating factor for the rate of melting. The present authors recently formulated a model in which the gas bubbles under the reacting batch are an integral part of the cold cap [11,12]. In this study, we have enhanced the initial simplified 1D cold cap model by including the dynamics of the foam layer. Also, we augmented the model by the formation of intermediate crystalline phases and the dissolution of quartz particles

[13]. Furthermore, we employed recent experimental studies of the properties of melting feed, such as heat capacity [14] and heat conductivity [15].

Our ultimate goal is to incorporate the cold cap model into the full waste-glass melter model. This will allow the melting rate to be estimated as a function of the feed formulation and melter operating conditions, thus helping to save the time and cost of the empirical development.

The particular melter feed chosen for this study has been formulated to vitrify one of the nuclear wastes considered for the Waste Treatment and Immobilization Plant, currently under construction at the Hanford Site. However, the paper is more focused on the model development than on a particular waste stream. Therefore, the methodology can be applied in any situation where a steady cold cap occurs.

The structure of the cold cap is described in Section 2, where the heat transfer through the foam layer and its impact on the rate of melting are described in detail. Section 3 summarizes the experimental data used in this work. The results are given in Section 4. Section 5 then addresses, among other topics, the route for the future implementation of the cold cap model into the model of the glass melter.

2. Theory

The cold cap model presented in this work rests on two simplifying assumptions. First, it is assumed that all feed components and evolving gases move, and that the heat flows, in the vertical direction. Thus, horizontal mass and heat flows are omitted. This assumption allows us to treat the feed-to-glass conversion within the cold cap as a 1D problem. Therefore, situations where some feed components move horizontally are not covered by the model. Second, we assume that all solids and liquids (molten salts and glass-forming melt) move with the same velocity. This allows us to treat the solid and liquid phases as a single condensed phase. Phenomena such as the reflux of volatiles or drainage of low-viscosity melt are not represented.

2.1 Cold cap structure

Fig. 1 illustrates the cold cap structure with its main regions: (i) open porosity layer, (ii) primary foam, (iii) cavities, and (iv) secondary foam. These regions were identified in reference [12] including the cavity layer (postulated in Sect. 5.5, but not shown in Fig. 1).

The boiling slurry keeps the top surface temperature, T_T, at ~ 100°C. Most of the cold cap reactions take place in the upper layer from which evolving gases freely escape through open pores. Open porosity closes when the glass-forming melt becomes connected at the primary foam temperature, T_P, at which first bubbles, initially of irregular shape, appear in the melt that encapsulates undissolved solids. Because of the high viscosity of the melt, the buoyant motion of the bubbles is slower than the downward motion of the melt and dissolving solid particles [12]. As the bubbles move down, they continue to grow as a result of gas-evolving reactions and increasing temperature.

At some critical temperature, T_C, the bubbles start to coalesce and merge with the large cavities below. The bottom temperature of the cavity layer, T_S, depends on the thickness of the secondary foam layer and on the bottom temperature, T_B, determined by the temperature and velocity field in the molten glass below the foam layer.

As mentioned above, the heat transfer through the foam layers from the melt to the cold cap influences the rate of melting and thus becomes a dominant factor for melter efficiency and the length of the lifecycle of the nuclear waste cleanup. The following 5 subsections (2.2 to 2.6) decribe the foam formation and its effect on the melting rate in detail. The final two subsections then outline the approach to the cold cap modeling.

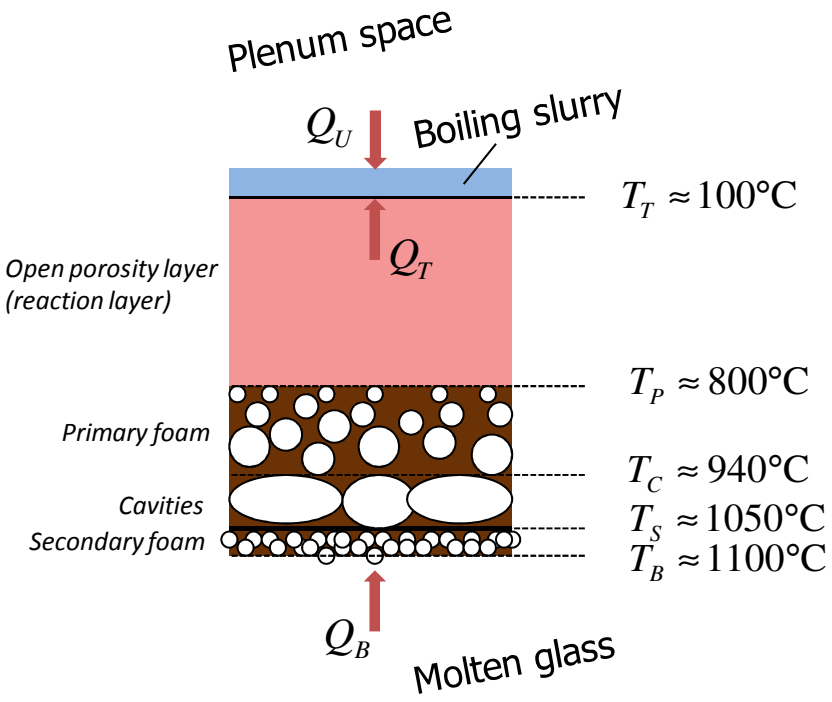

Fig. 1. Schematic illustration of a cold cap displaying typical cold cap layers.

2.2 Primary foam

The T_P is identifiable as the local minimum and the T_C as the maximum on the feed expansion curve, Fig. 2 [12]. The foam expansion curve was produced by measuring the profile area of feed pellets heated at a constant temperature-increase rate. The increase in the profile area above T_P is caused by the formation and growth of gas bubbles. The T_C increases with increasing heating rate. For feed with quartz grain size 45 µm, we fitted the T_c versus β with the power-law function $T_C/°C = 839\beta^{0.058}$, where β (K min^{-1}) is the heating rate.

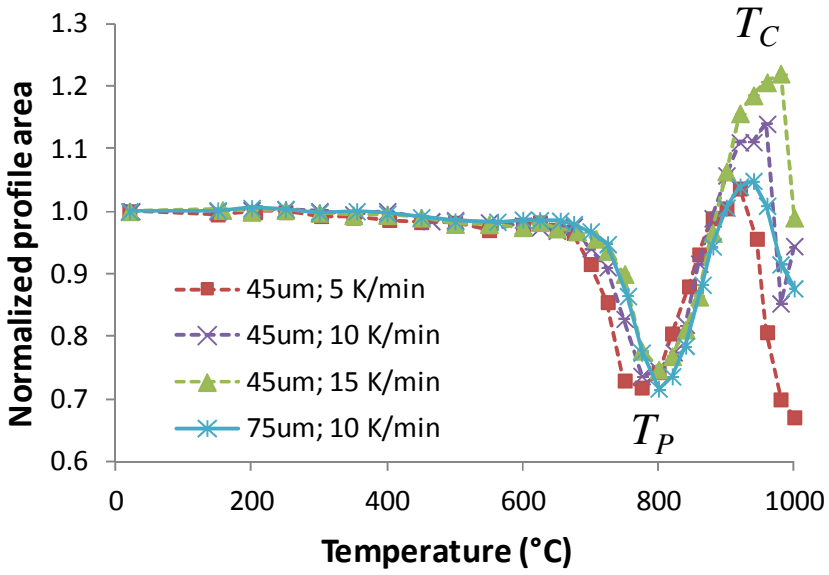

Fig. 2. Normalized melter-feed-pellet profile area versus temperature measured for various heating rates and quartz grain sizes.

2.3 Cavities

The shape of a gas-filled cavity trapped in a quiescent liquid under a horizontal downward-facing solid surface is determined by capillary forces [16]. Under the cold cap, the cavities are sandwiched between two foam layers. Bubbles from the foam layers burst into the upper and lower surfaces of the cavities. Though such cavities can hardly be described as bodies of gas in quiescent liquid under a solid surface, their thickness is determined at their edges which interface with molten glass. Unless obstructed horizontally, cavities are flat discs. In a typical molten glass, their thickness is ~7 mm [12].

Generally, thin cavities do not possess sufficient buoyancy to force the accumulated gas vertically through the cold cap. Instead, the gas cavities, or the gas in stagnant cavities, move sideways to the edges of the cold cap and to vent holes (openings in the cold cap), where the gas is released to the plenum space. The vent holes appear as local disturbances in the cold cap or are created by big bubbles from bubblers submerged in the molten glass. When obstructed horizontally, cavities can grow vertically without limits. This happens when the cold cap touches the melter wall, an event that normally does not occur and cannot be captured in the 1D model. Also, the 1D model does not portray the horizontal motion of cavities, which are treated as sinks of the gas liberated from the foam layers.

Assuming that the cavities have a shape of flat circular discs arranged in a hexagonal matrix, they ideally cover ~90% of the cold cap area (the coverage ratio being $p = \frac{1}{2}\pi/\sqrt{3}$), leaving ~10% of the cold cap area for molten glass to flow down in the columns ten times faster than melt flows in the absence of the gas phase. These columns plunge through secondary foam, which, unless disturbed by bubblers (see Sect. 5.4), is solid-like and relatively still.

2.4 Secondary foam

Secondary foam is formed by bubbles from redox reactions in the molten glass. The thickness of the secondary foam, h_s, is governed by fluid mechanics as discussed in [17]. The foam height is

$$h_s = \Phi j_{sg} \tag{1}$$

where j_{sg} is the volumetric gas-phase flux entering the secondary foam from the melt and Φ is a constant called the foaminess; as follows from this equation, foaminess is a measure of the extent of foaming response of the liquid to the superficial gas flow [18]. The j_{sg} is related to the condensed phase flux (the rate of melting, j_M) as

$$j_{sg} = k j_M \tag{2}$$

For melt with a single multivalent oxide, such as Fe_2O_3, the oxide becomes increasingly reduced as the melt temperature grows while it circulates in the melter. Then

$$k = g_0 f_r \frac{RT}{\nu M_0 P} \tag{3}$$

where g_0 is the oxide mass fraction, f_r is the oxide reduced fraction, M_0 is the oxide molecular mass, ν is the stoichiometric coefficient, R is the universal gas constant, and P is the pressure. Note that k has a dimension $m^3\ kg^{-1}$, because j_{sg} is in $m\ s^{-1}$, whereas j_M is in $kg\ m^{-2}\ s^{-1}$.

A combination of Eqs. (1) and (2) gives a linear relationship between the melting rate and secondary foam thickness:

$$h_s = k\Phi j_M \tag{4}$$

Thus, at a higher melting rate, more bubbles are created in molten glass (Eq. (2)). A higher flux of ascending bubbles produces a thicker secondary foam layer (Eq. (4)), resulting in a lower T_S (as described in section 2.5).

In our study, the source of secondary foam gas is Fe_2O_3 (see Section 3.1):

$$2Fe_2O_3 \rightarrow 4FeO + O_2 \tag{5}$$

For a small reduced fraction (0.04 is a typical value), we can write, $f_r \approx$ Fe(II)/Fe(III). The redox ratio is related to temperature as [19]

$$\ln(f_r) = A - B/T \tag{6}$$

where $A = 5.05$ and $B = 1.21 \times 10^4$ K. For $T = 1150$°C, $f_r = 0.032$. Since $M_o = 208$ g mol^{-1}, $\nu = 2$, $R = 8.31$ J mol^{-1} K^{-1}, $P = 1.01 \times 10^5$ Pa, and $g_0 = 0.059$ (see section 3.1). Thus, we have, by Eq. (3), $k = 5.26 \times 10^{-4}$ m^3 kg^{-1}.

2.5 Heat transfer through foam layer

The heat flux, q, transferred through the foam layer determines the melting rate. According to Fourier's law, $q = \lambda_i^{Eff}\Delta T_i/h_i$, where λ^{Eff} is the effective heat conductivity, ΔT is the temperature difference across the layer, h is the layer thickness, and subscript i represents primary ($i \equiv p$) or secondary ($i \equiv s$) foam layer. The heat is transferred across the cavity layer by both conduction, $q_{c,cond} = \lambda_c(T_S - T_C)/h_c$, and radiation, $q_{c,rad} = \sigma(T_S^4 - T_C^4)/(2/\varepsilon - 1)$, where λ_c is the heat conductivity of the melting feed in the cavity, h_c is the cavity layer thickness, ε is the emissivity, and $\sigma = 5.670373 \times 10^{-8}$ Wm^{-2}K^{-4} is the Stefan-Boltzmann constant. For simulations, we used $\varepsilon = 0.88$, reported for molten glass by Viskanta and Wu [6]. Neglecting the contribution of the conductive heat transfer in the gas phase, we have $q = pq_{c,cond} + (1 - p)q_{c,rad}$. The surface coverage ratio is set to $p = 0.15$ in our simulations.

Because the thicknesses of foam layers are controlled by liquid film stability and the thickness of the cavity layer is given by capillarity, smaller ΔT_is are not automatically compensated by smaller h_is.

According to Fourier's law, $q = \lambda_s(T_S - T_B)/h_s$, and by Eq. (4), the higher melting rate (and corresponding higher heat flux) results in a decreased T_S. Thus, a higher melting rate causes a simultaneous increase of T_C and decrease of T_S, reducing the temperature difference ($T_S - T_C$) across the cavity layer and decreasing the heat flux to the cold cap, hence decreasing the melting rate. Accordingly, a melting rate exists at which the steady-state temperature gradient across the cavity layer, $(T_S - T_C)/h_c$, corresponds to the constant rate of melting. If the feed is charged to the melter faster, not enough heat will be supplied across the foam layer and the cold cap will spread to the melter walls. If the feeding rate is slower, the cold cap will shrink.

2.6 The algorithm for estimation of melting rate

Neglecting the heat consumed in the foam layer, the heat q transferred across foam layers is constant, thus

$$q = q_i \text{ for } i \equiv p, c, s \tag{7}$$

which gives us a set of three linearly dependent equations, from which we can choose two independent, for example,

$$\begin{aligned} &\lambda_p(T_P - T_C)/h_p = pq_{\text{c,cond}} + (1-p)q_{\text{c,rad}} = (1-p)\lambda_{\text{cavity}}(T_S - T_C)/h_{\text{c}} + p\sigma(T_S^4 - T_C^4)/(2/\varepsilon - 1) \\ &\lambda_p(T_P - T_C)/h_p = \lambda_s(T_S - T_B)/h_s \end{aligned} \tag{8}$$

Because h_{c} is determined by capillary forces and h_s by Eq. (4), the T_S, h_p, and q can be obtained from the solution of Eq. (8).

The condensed-phase mass flux, j_T, at the cold cap top is related to the heat flux q as

$$j_T = \frac{q}{H_{melt} + (1 - f_{plenum})H_{slurry}} \tag{9}$$

where $H_{melt} = \int_{T_T}^{T_B} c_b^{Eff}\, dT$ is the heat necessary to raise the dry feed temperature from 100°C to 1100°C, H_{slurry} is the heat to turn the slurry fed to the melter into dry feed at 100°C, f_{plenum} is the fraction of this heat supplied to the cold cap from the plenum space, and c_b^{Eff} is the effective heat capacity. Thus, the larger is the fraction of water evaporated from slurry by the heat supplied from above, the higher is the melting rate at a constant heat flux across the foam layer.

2.7 Cold cap energy balance

The energy balance of the cold cap can be written in the following form [12]:

$$\rho_b c_b \frac{dT}{dt} = \left(j_b c_b^{Eff} - j_g c_g\right)\frac{dT}{dx} - \lambda^{Eff}\frac{d^2T}{dx^2} \tag{10}$$

where ρ is the spatial density, c is the effective heat capacity, t is the time, j is the mass flux, x is the spatial coordinate (vertical position), and the subscripts b and g denote the condensed phase and the gas phase, respectively. The effective heat capacity of the condensed phase, c_b^{Eff}, includes the heat from melting reactions (such as evaporation of bonded water, etc.); see Section 3.3. The effective heat conductivity is assumed to involve both conductive and radiative modes of heat transfer in the feed (see Section 3.5).

The condensed-phase mass flux within the cold cap is calculated as $j_b = \alpha_b j_T$, where α_b is the mass fraction of condensed phase (see Section 3.2) and j_T is the mass flux of dry feed entering the cold cap. The total amount of evolved gas is $\Delta j_b = j_T - j_M$, where j_M is the condensed-phase mass flux leaving the cold cap (melting rate). Thus, the gas-phase mass flux can be calculated as $j_g = (\alpha_b - \alpha_M)j_T$, where α_M is the mass fraction of condensed phase at the cold cap bottom.

The energy balance equation was processed by finite volume method [15], using 150 finite volumes. Considering the average cold cap thickness ~3 cm, the discretization step was ~0.2 mm. The algorithm was coded in Mathworks® MATLAB 7.

2.8 Model iteration

The procedure for the incorporation of the foam layer model into the model of the cold cap is as follows:

i) The initial melting rate and foam layer temperatures (T_C, T_S) are chosen.
ii) The thickness of the cold cap is calculated by the model based on the chosen melting rate and foam layer temperatures (T_C, T_S).
iii) The average heating rate of the feed is calculated from the obtained time-temperature history of the feed in the cold cap.
iv) Based on the average heating rate, the foam layer model updates the amount of heat transferred through the foam layer together with the layer temperatures (T_C, T_S).
v) The new melting rate for the cold cap model is calculated from the heat transferred through foam.
vi) The temperatures of the foam layer in the cold cap model (T_C, T_S) are updated from the foam layer model.
vii) The process is repeated from step ii) until the difference between the amount of heat transferred through the foam layer and the heat necessary for melting is small, indicating that a steady-state melting rate was reached.

3. Experimental

3.1 Melter feed

Table 1 shows the composition of the melter feed used in our study, denoted as A0, which was also used for the initial modeling of the cold cap [12]. It represents a simplified version of a batch designed for the Hanford Waste Treatment and Immobilization Plant [20]. This simplified version was formulated to produce a glass of the following composition (with mass fractions in parentheses): SiO_2 (0.305), Al_2O_3 (0.240), B_2O_3 (0.152), Na_2O (0.096), CaO (0.061), Fe_2O_3 (0.059), Li_2O (0.036), Bi_2O_3 (0.011), P_2O_5 (0.011), F (0.007), Cr_2O_3 (0.005), PbO (0.004), NiO (0.004), ZrO_2 (0.004), SO_3 (0.002), K_2O (0.001), MgO (0.001), and ZnO (0.001). The simulated batch was prepared, as described by Schweiger et al. [20], as slurry that was dried at 105°C overnight in an oven. The properties of this batch have been well, although not completely, characterized [21,22,23]. To study the variation of the alumina source on the melting rate, we also performed simulations on feed containing AlO(OH), boehmite, as an alumina source instead of $Al(OH)_3$.

Table 1. Melter feed composition (in g) to make 1 kg of glass A0

Compound	g
$Al(OH)_3$	367.49
H_3BO_3	269.83
CaO	60.79
$Fe(OH)_3$	73.82
Li_2CO_3	88.30
$Mg(OH)_2$	1.69
NaOH	99.41
SiO_2	305.05
$Zn(NO_3)_2{\cdot}4H_2O$	2.67

$Zr(OH)_4 \cdot 0.65H_2O$	5.49
Na_2SO_4	3.55
$Bi(OH)_3$	12.80
Na_2CrO_4	11.13
KNO_3	3.04
$NiCO_3$	6.36
$Pb(NO_3)_2$	6.08
$Fe(H_2PO_2)_3$	12.42
NaF	14.78
$NaNO_2$	3.37
$Na_2C_2O_4$	1.26
Total	1349.32

3.2 Mass fraction of condensed phase

The kinetics of batch reactions that result in a change in the condensed-phase content was addressed in [24]. As in our previous paper [15], we disregarded the effect of the changing heating rate on the conversion kinetics. Instead, up to 700°C, we approximate the $\alpha_M = f(T)$ function measured with thermogravimetric analysis (TGA) at a constant heating rate 20 K min^{-1} as

$$\alpha_b = \alpha_0 - \alpha_1 \arctan\left(\frac{T - T_1}{T_2}\right) \qquad (T < 973 \text{ K}) \qquad (11)$$

For the feed with $Al(OH)_3$, $\alpha_0 = 0.906$, $\alpha_1 = 0.081$, $T_1 = 588.6$ K, and $T_2 = 92.42$ K. For the feed with AlO(OH), $\alpha_0 = 0.918$, $\alpha_1 = 0.068$, $T_1 = 699.1$ K, and $T_2 = 153.7$ K. The comparison of the measured TGA curves and the fitted α_bs for both feeds is displayed in Fig. 3.

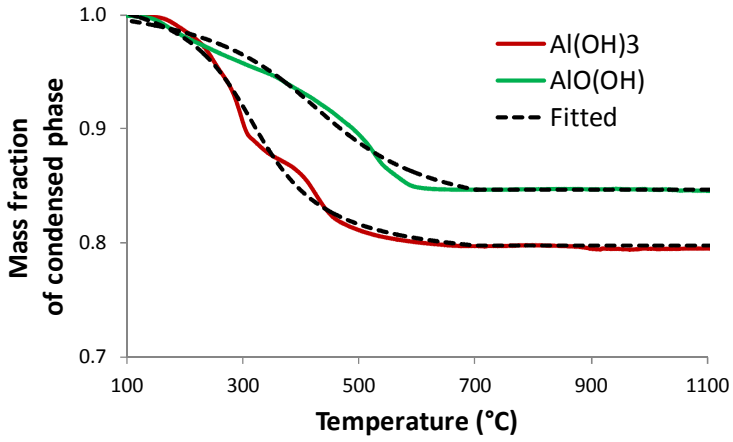

Fig. 3. Measured and fitted mass fractions of condensed phase versus temperature at 20 K min^{-1} heating rate for feeds with $Al(OH)_3$ and AlO(OH).

3.3 Heat capacity

The peaks on the effective-heat-capacity curves, Fig. 4, are associated with endothermic reactions, such as the release of bonded water or decomposition of carbonates. The c_b^{Eff} is the sum of the specific heat, c_b, and the reaction heat, i.e., [14]

$$c_b^{Eff} = c_b + \Delta H \mathrm{d}\alpha_H/\mathrm{d}T \quad (12)$$

where ΔH is the total reaction heat (J kg^{-1}) and α_H is the degree of conversion related to reaction heat. The reaction heat term, $\Delta H \mathrm{d}\alpha_H/\mathrm{d}T$, was obtained using the kinetic parameters for heating rate 20 K min^{-1} [14]. For the feed with AlO(OH), the c_b^{Eff} was determined experimentally. After the reactions were completed at ~600°C, the c_b^{Eff} assumed a nearly constant value of 1100 J kg^{-1} K^{-1} for both feeds.

The heat to turn the slurry fed to the melter into dry feed at 100°C, see Eq. (9), was calculated from slurry drying experiments to be $H_{slurry} = 3.31 \times 10^6$ J kg^{-1} of dry feed with Al(OH)$_3$ and $H_{slurry} = 3.64 \times 10^6$ J kg^{-1} of dry feed with AlO(OH).

Following Schill [10], the heat capacity of the gas phase was approximated by that of carbon dioxide:

$$c_g(T) = 1003 + 0.21T - \frac{1.93 \cdot 10^7}{T^2} \quad (c_g \text{ in J kg}^{-1}\text{K}^{-1} \text{ and } T \text{ in K}, T \geq 373 \text{ K}) \quad (13)$$

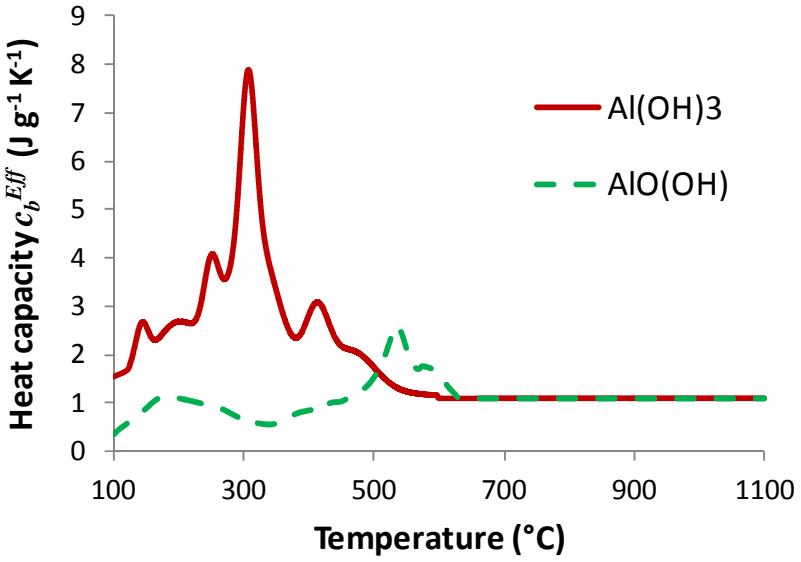

Fig. 4. Effective heat capacities versus temperature for melter feeds with Al(OH)$_3$ (solid line) and AlO(OH) (dashed line) heated at 20 K min^{-1}.

3.4 Density (including expansion measurements)

The melter feed bulk density was estimated from pellet expansion data (displayed in Fig. 2) and from the loose-batch data reported in [19]. The volumes of both loose batch and pellets changed little initially while batch gases evolved. Gases were escaping through open pores even while melter feed was shrinking, starting at ~700°C to a minimum volume at T_P. Above T_P, the glass-forming melt became connected and open pores turned into bubbles while gases continued to evolve. As temperature increased, the melt expanded to foam that eventually collapsed at T_C.

As described by Henager et al. [22], the normalized area, shown in Fig. 2, was converted to the volume, thus allowing the calculation of the void fraction and the density. The initial density of loose melter feed was $\rho_{b0} = 970$ kg m^{-3} [19]. The density decreased with increasing temperature as a result of mass loss and the nearly constant volume of the sample at $T <$ ~700°C, i.e., $\rho_b(T) = \rho_{b0}\alpha_b$. Once the sample was shrinking between ~700 and 800°C, the density increased to a maximum of 1.205×10^3 kg

m^{-3}. It can be assumed that the bulk density and porosity were not affected by the initial compression of pellets at and above the minimum-volume temperature, T_P. Then, above T_P, the density decreased as the bubbly melt turned to foam, reaching a minimum. For a heating rate of 15 K min^{-1}, the minimum density of 541 kg m^{-3} was reached at ~960°C when the void fraction increased to an unsustainable value of 0.79.

The spatial density of the cavity layer, ρ_C, can be calculated as $\rho_C = p\rho_M$, where p is the coverage ratio defined in Section 2.5 and $\rho_M = 2.5 \times 10^3$ kg m^{-3} is the molten glass density. Thus, with $p = 0.15$, $\rho_C = 375$ kg m^{-3}. Whereas the feed density has a crucial impact on the condensed-phase velocity and heating rate, thus affecting the T_C as explained in Section 2.2, the values of ρ_C and the spatial density of secondary foam, ρ_S, do not significantly affect the simulation results. This is because the average heating rate the feed is experiencing in the cavity and secondary foam regions do not affect the behavior of layers above. For simplicity, we assumed that ρ_S and ρ_C have the same value.

3.5 Heat conductivity

Fig. 5 displays λ_c^{Eff} as a function of temperature. The λ_c^{Eff} of the reacting feed was estimated using the relationship [15]

$$\lambda^{Eff} = 0.233 + 4.70 \times 10^{-5} T \qquad (\lambda \text{ in W m}^{-1}\text{ K}^{-1} \text{ and } T \text{ in K}, 373\text{ K} < T < 973\text{ K}) \qquad (14)$$

Based on the extrapolation of data provided in [15], we estimated the primary foam conductivity to be $\lambda_P = 1$ W m^{-1} K^{-1} (from T_P to T_C). Considering the values provided for molten glass in [25], the heat conductivity of the melt in the cavity was estimated to be $\lambda_{cavity} = 4$ W m^{-1} K^{-1}. Secondary foam conductivity was estimated to be $\lambda_S = 2$ W m^{-1} K^{-1} (from T_S to T_B). The effective heat conductivity of the cavity layer, $\lambda_c^{Eff} = qh_c/(T_S - T_C)$, was iteratively calculated because it depends also on the contribution of radiation. The values of λ_c^{Eff} typically varied between 2 and 2.5 W m^{-1} K^{-1}.

Relationship (14) is valid up to 700°C (973K), at which point the heat conductivity starts to differ significantly from the linear trend [15]. As the feed expansion curve, Fig. 2, shows, the feed density begins to decrease at ~700°C, resulting from the shrinkage caused by the development of glass-forming melt. Consequently, λ_c^{Eff} increases until foam begins to develop at T_P. As indicated in Fig. 5, we used a linear transition to bridge the gap between the λ_c^{Eff} at $T < 700$°C and λ_P. A detailed study of foam heat conductivity is underway. Because of its complexity and extent, it will be addressed in a separate communication.

The constant heat conductivities of the foam layers significantly simplified the iterative calculation of heat flux through the foam. The effective heat conductivity in the cavity layer (from T_C to T_S), which was not constant in the simulations, is marked by the dashed line in Fig 5.

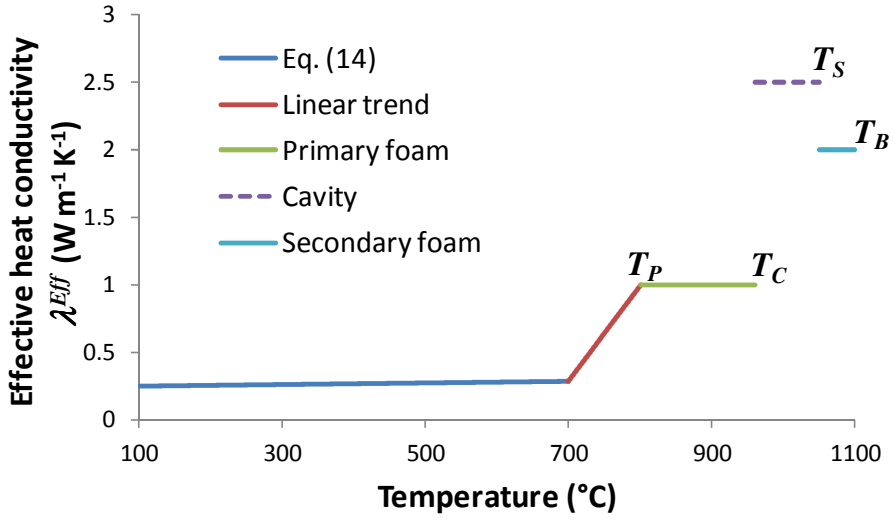

Fig. 5. Melter-feed effective heat conductivity versus temperature.

4. Results

The simulation parameters were T_B, h_C, f_{plenum}, and Φ. By varying their values, we examined their effects on the melting rate and cold cap properties. Their baseline values were T_B = 1100°C, h_C = 7 mm, f_{plenum} = 0.5 (the fraction of heat from above), and Φ = 400 s [8].

4.1 Effects of cold cap bottom temperature and feed foaminess on cold cap properties

Figs. 6–9 display the dependence of the melting rate, secondary foam thickness, top and bottom cavity temperatures (T_C and T_S), and cold cap thickness on the cold cap bottom temperature for various values of foaminess (shown in the legend). The melting rate and both T_C and T_S increase and cold cap thickness decreases with increasing T_B and decreasing Φ. As expected from Fourier's law, $q = \lambda\Delta T/h$, and Eq. (9), the cold cap thickness is inversely proportional to the melting rate.

The secondary foam thickness increases with increasing T_B and increasing Φ. As Fig. 7 shows, a melt with the level of foaminess as low as Φ = 100 s would produce a secondary foam layer that is less than 1 mm thick. With bubbles of 1 mm diameter, this would mean virtually no foam. The value of Φ = 400 s would result in a monolayer of bubbles and the melt of Φ = 1000 s would generate a ~3 mm layer of secondary foam. These values would increase for glasses containing more iron oxide; for example, they would double for a melt containing 11 mass% Fe_2O_3. Consequently, for a high-iron glass, foaminess would affect the rate of melting significantly more than Fig. 6 indicates. Foaminess, or the propensity of the melt to foam, depends on foam stability, which is a function of glass composition, presence of solid inclusions, and viscosity.

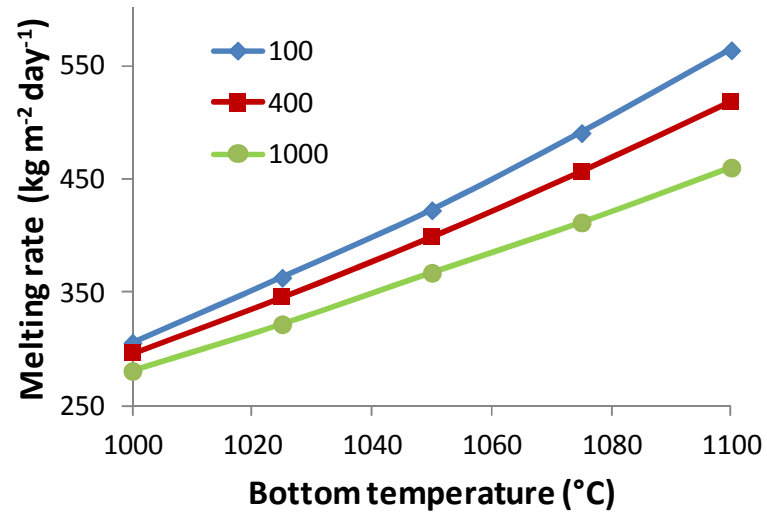

Fig. 6. Melting rate versus cold cap bottom temperature and foaminess (values in the legend).

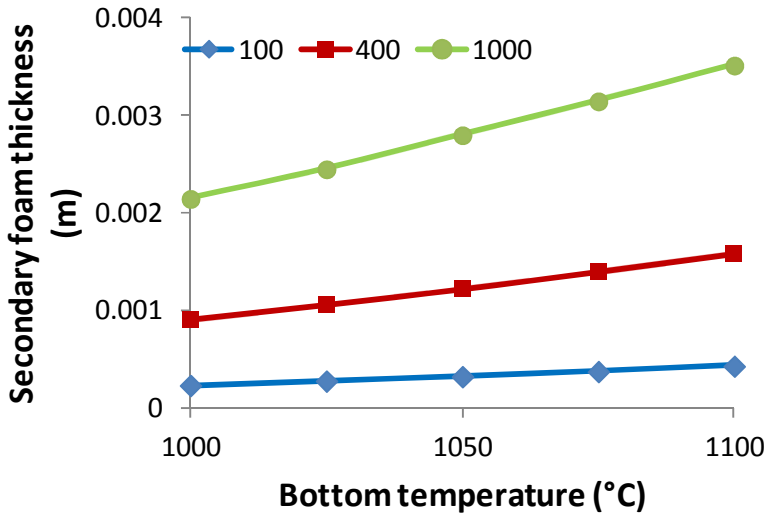

Fig. 7. Secondary foam layer thickness versus cold cap bottom temperature and foaminess (values in the legend).

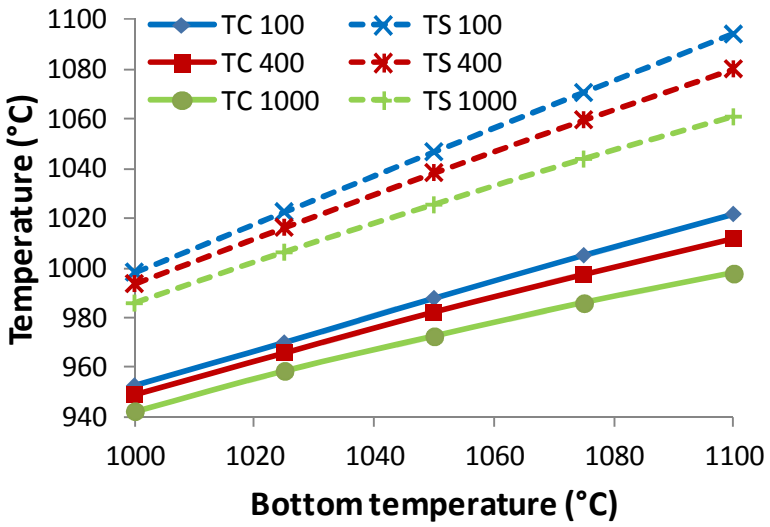

Fig. 8. Cavity layer boundary temperatures versus cold cap bottom temperature and foaminess.

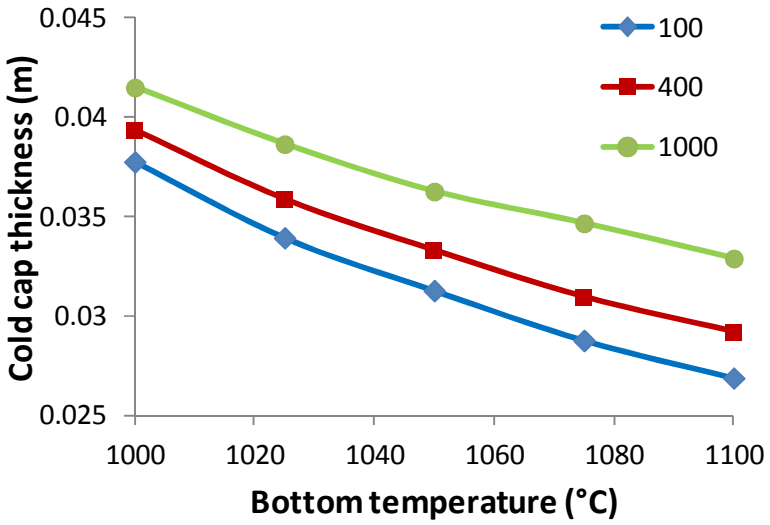

Fig. 9. Cold cap thickness versus cold cap bottom temperature and foaminess.

4.2 Effects of cold cap bottom temperature on profiles of temperature, condensed phase velocity, and heating rate

Figs. 10–12 display calculated profiles of temperature, velocity, and local heating rate with respect to the position in the cold cap (recollect that $h = 0$ correspond to the cold cap top) for $T_B = 1100$°C and 1050°C. The temperature profiles (Fig. 10) exhibit three intervals with distinct temperature gradients. Starting from the cold cap top, the interval from 100°C to 800°C pertains to the open porosity layer with a steep temperature gradient caused by the low effective heat conductivity of the feed. Below the open porosity layer, the temperature gradient decreases in the primary foam region and then further in the cavity and secondary layers. No significant change in temperature gradient is noticeable between the cavity layer and secondary foam layer.

The velocity profile displayed in Fig. 11 closely follows the evolution of density. The minimum condensed-phase velocity occurs just above the foam layer, where the porosity of the feed reaches its minimum. In the foam layers, the velocity then increases as a result of decreasing foam density.

The profile of heating rate (Fig. 12) was locally evaluated in each finite volume from the temperature difference across the adjacent finite volume and the time feed spends in it. It initially increases as the fraction of condensed phase decreases, with the fastest increase at ~300°C, where most of the gas-evolving reactions take place. Then, it sharply drops when the melt becomes connected and the heat conductivity rises (see Fig. 5). Then it slightly increases again in the primary foam region and again sharply decreases when foam coalesces and collapses.

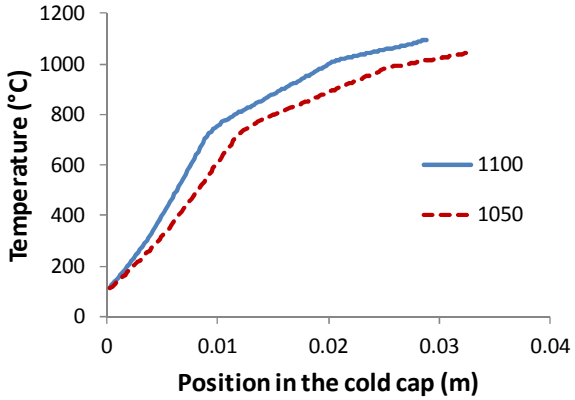

Fig. 10. Temperature profile within the cold cap for two cold cap bottom temperatures.

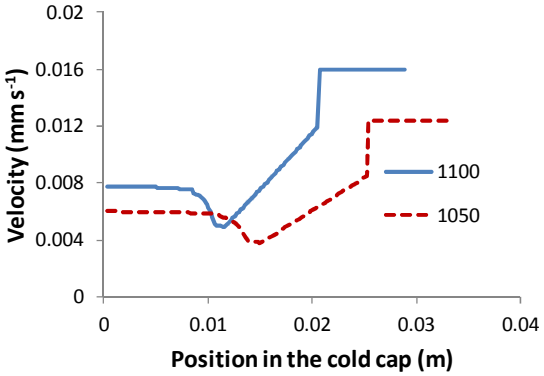

Fig. 11. Condensed-phase velocity profile within the cold cap for two cold cap bottom temperatures.

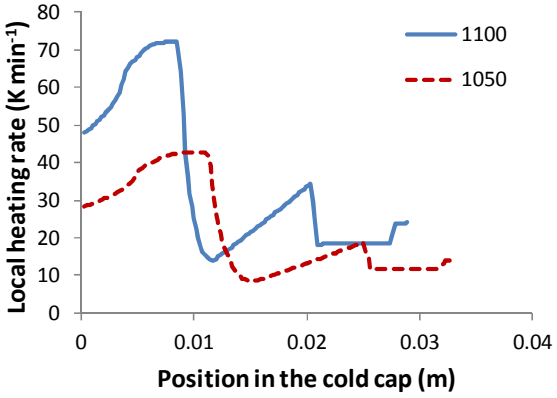

Fig. 12. Heating rate profile within the cold cap for two cold cap bottom temperatures.

4.3 Quartz distribution within the cold cap

Poorly dissolved and incompletely homogenized silica can have a detrimental impact on high-level-waste (HLW) glass durability because the low-silica matrix glass has a decreased resistance to corrosion by water [13]. Thus the quartz dissolution within the cold cap and size of the quartz particles leaving the cold cap are of concern.

The amount of undissolved quartz within the cold cap was obtained using the *n*th order model for quartz dissolution [13]:

$$\frac{\mathrm{d}c_Q}{\mathrm{d}t} = A(1-c_Q)^n \exp\left(-\frac{B}{T}\right) \tag{15}$$

where c_Q is the fraction of dissolved quartz, A is the pre-exponential factor, $n = 1.36$ is the (apparent) reaction order, and $B = E/R = 9.46 \times 10^3$ K, where E is the activation energy. The A value is a function of β as $A = A_0(1 + \beta/\beta_0)$, where $A_0 = 2.257$ s^{-1} and $\beta_0 = 4.752$ K min^{-1}.

The amount of dissolved quartz was calculated in each finite volume. Fig. 13 displays the amount of undissolved quartz as a function of temperature in the cold cap for cold cap bottom temperatures of 1050°C and 1100°C. Although the rapid heating rate in the open porosity layer results in a large fraction of undissolved quartz initially, the slow local heating rate above 700°C provides enough time for almost complete quartz dissolution. Yet a small fraction of quartz enters the molten glass below: 1.9% for $T_B = 1050$°C and 1.2% for $T_B = 1100$°C. At a cold cap temperature of 1050°C, the undissolved quartz fraction is higher for $T_B = 1100$°C (2.3%) than for $T_B = 1050$°C; this is caused by a lower local heating rate at $T_B = 1050$°C (see Fig 12). Considering the initial quartz particle size of 75 μm, the average sizes of particles leaving the cold cap are ~20 μm and ~16 μm for $T_B = 1050$°C and 1100°C, respectively. These values are close to the 15–30 μm sizes of quartz grains that were leaving the cold cap in the laboratory-scale melter [13].

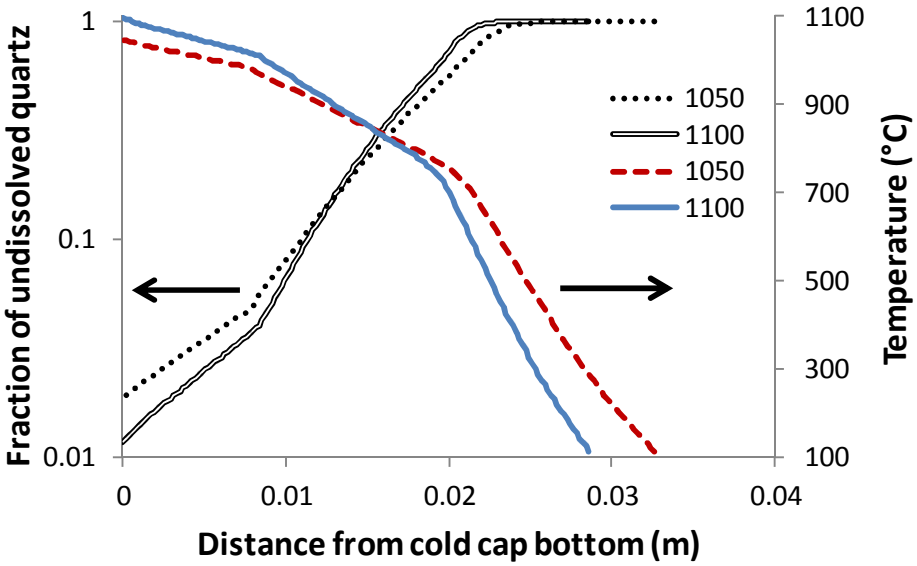

Fig. 13. Fraction of undissolved silica within the cold cap for two values of cold-cap bottom temperature indicated in legend.

4.4 Hematite and spinel distribution within the cold cap

The presence of spinel affects the HLW melter processing via settling, particularly in the melter discharge riser during idling periods [26]. The initial fraction and size of spinel crystals entering melt convection currents in the melt beneath the cold cap affects their fate inside the melter. Spinel settling can be avoided if the crystals are small enough to remain suspended in glass.

The fraction of crystalline hematite and spinel within the cold cap was obtained using the model for spinel behavior [13]. Spinel originating from hematite dissolves when its concentration exceeds the equilibrium. Thus [13]

$$\frac{\mathrm{d}\,c_s}{\mathrm{d}\,t} = -p_{hs}\frac{dc_h}{dt} + 2k_H n_s\left(c_{s0} - c_s\right) \tag{16}$$

where c_s is the spinel fraction, p_{hs} is the hematite-to-spinel ratio, c_h is the hematite fraction, k_H is the Hixson-Crowell rate constant, n_s is the crystal-number density, and c_{s0} is the equilibrium spinel fraction. Using data provided in [23], $p_{hs} = 1$, $c_h = 0.0186\{1 - \tanh[(T - 1008)/(122.9)]\}$, $c_{s0} = 0.047\{1 - \exp[1/T - 1/1572]\}$, where T is in K, and the $k_H n_s$ value is a function of β (K min^{-1}) $k_H n_s = K_0(1 + \beta/\beta_1)$, where $K_0 = 1.375 \times 10^{-2}$ s^{-1} and $\beta_1 = 2.08$ K min^{-1},

Fig. 14 displays the fraction of crystalline hematite within the cold cap, together with the spinel fraction calculated using Eq. (16). The procedure for the calculation was the same as that for undissolved quartz.

The fraction of spinel in the melt leaving the cold cap is 3.0 mass% (corresponding to 0.98 vol%) for T_B = 1050°C and 2.6 mass% for T_B = 1100°C. The equilibrium fraction is ~1 mass% at 1150°C, which is close to the fraction at which the melt will leave the melter.

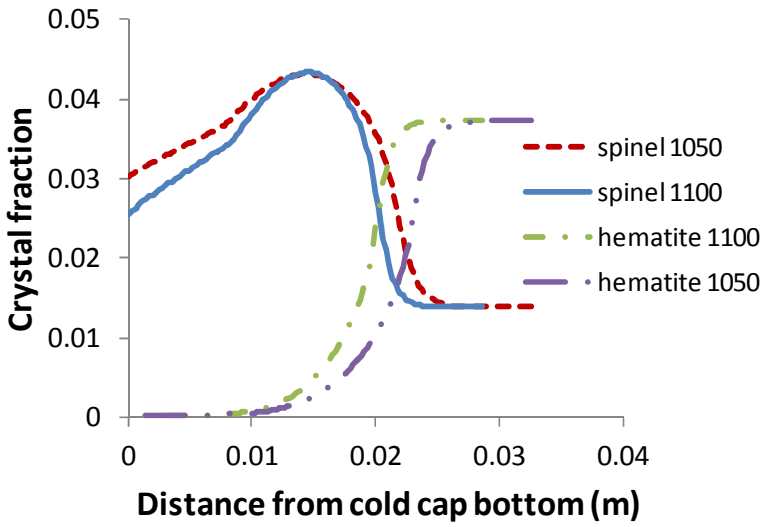

Fig. 14. The crystal fraction profiles within the cold cap for two values of cold-cap bottom temperature indicated in legend.

4.5 Effect of alumina source on melting rate

The chemical form of batch components affects the melting heat and melting rate. Therefore, the batch makeup has a decisive effect on the economy and efficiency of both commercial [27] and waste glass production [28].

Fig. 15 displays the dependence of the melting rate on the f_{plenum} (see Eq. 9) for feeds containing two alumina sources, gibbsite ($Al(OH)_3$) and boehmite (AlO(OH)). The f_{plenum} (to be determined by the model of whole glass melter) is a function of melter conditions and depends on the plenum space temperature. While the expansion (foaming) curves of both feeds are similar, the higher melting rate of AlO(OH) feed, ~15% for f_{plenum} = 0.3 and ~25% for f_{plenum} = 0.7 (Fig. 15), is caused by its considerably lower conversion heat (see Fig. 4). This is in agreement with the melter experiments [28]; the feed with AlO(OH) as the alumina source melted up to 25% faster than the feed with $Al(OH)_3$.

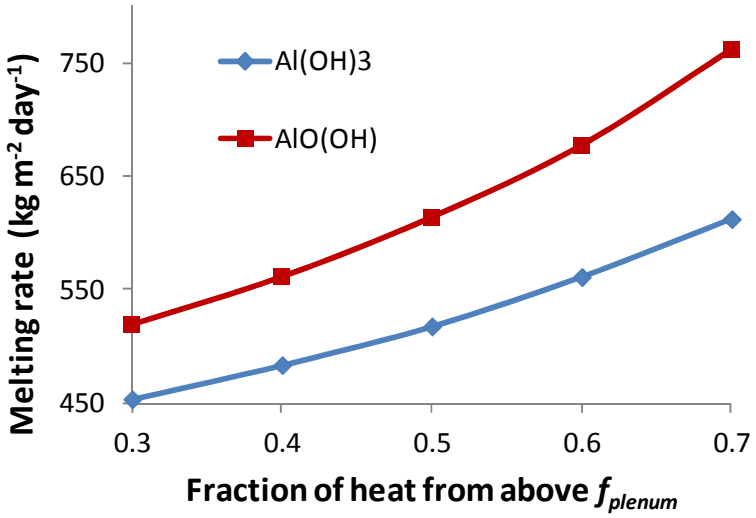

Fig. 15. Melting rate versus fraction of heat supplied from above for feeds with different alumina sources.

5. Discussion

The ultimate objective of this work is to develop a model for the cold cap that will account for important factors affecting its behavior. Such a model will, once incorporated in the model of the glass melter, be able to estimate the melting rate as a function of feed properties and melter operating conditions. In this study, we have developed an advanced version of such a model, which includes the behavior of the foam layer. Limitations of this model are discussed below together with the key factors to be accounted for in the glass melter model. Also included are recommendations for the future development of the cold cap model.

5.1 Cavity layer

While experimental data of cavity thickness, size, shape, coverage ratio, and motion are still incomplete, various observations evidence that the cavity layer is a part of the cold cap structure. Bursting of large bubbles is being observed at the cold cap edges and in the vent holes [29]. In the absence of cavities, cold cap edges and vent holes would contain copious amounts of foam, which is not the case. Also, the fast collapse of foam (see Fig. 2), after the foaming curve reaches maximum, supports the idea of a rapid coalescence of foam bubbles into cavities, as discussed in Section 2. Finally, large bubbles merging into cavities can be seen in cold cap samples from the laboratory-scale melter, Fig. 16 [30]. Large cavities, potentially leading to cold cap bridging, were observed by x-ray tomography of melter feeds heated from below (taken at Savannah River National Laboratory [31]), Fig. 17. And cavities are frequently observed in crucibles with melts quenched from the foaming temperature (Fig. 18).

The horizontal motion of cavities should not present a serious problem for the 1D modeling of the cold cap. First, approximately two thirds of the total heat flux across the cavity is transferred by radiation, depending solely on the top and bottom temperatures of the cavity. Second, the volume of gas released from the cold cap is 10^3 to 10^4 larger that the volume of glass produced. Only tiny fraction of this volume is released into the cavities. Hence, the horizontal flow of mass and heat caused by the cavity motion represents a negligible sink in 1D model.

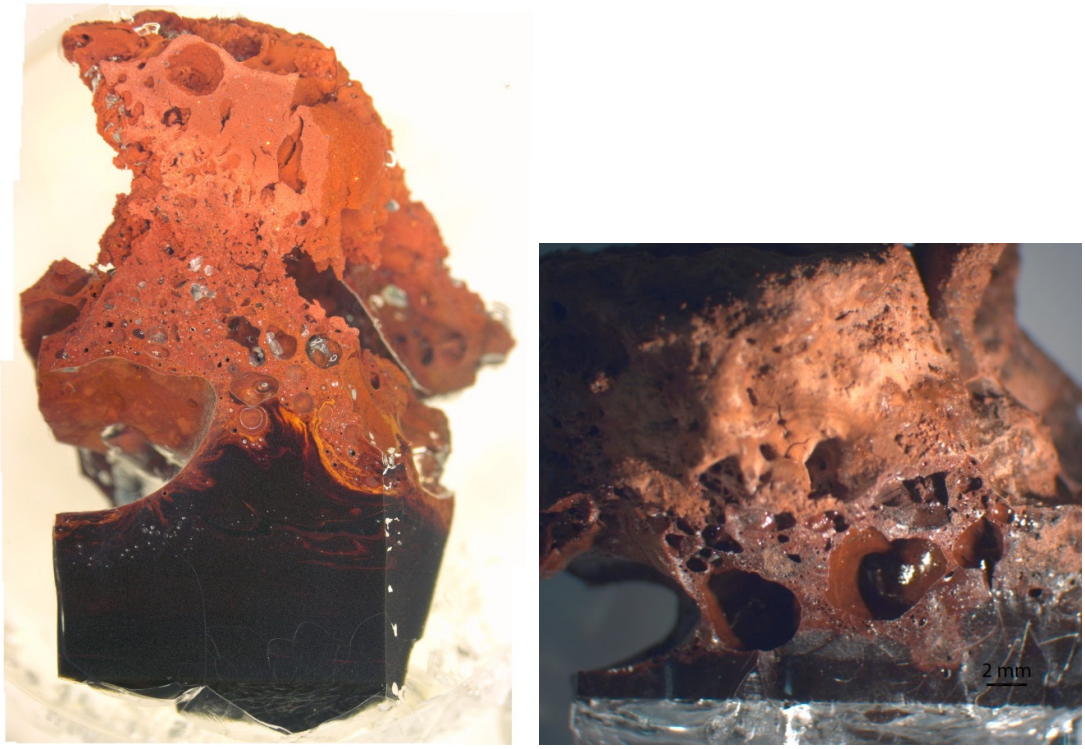

Fig. 16. Fracture surfaces of cold caps formed in a laboratory-scale melter showing large cavities from coalescing bubbles.

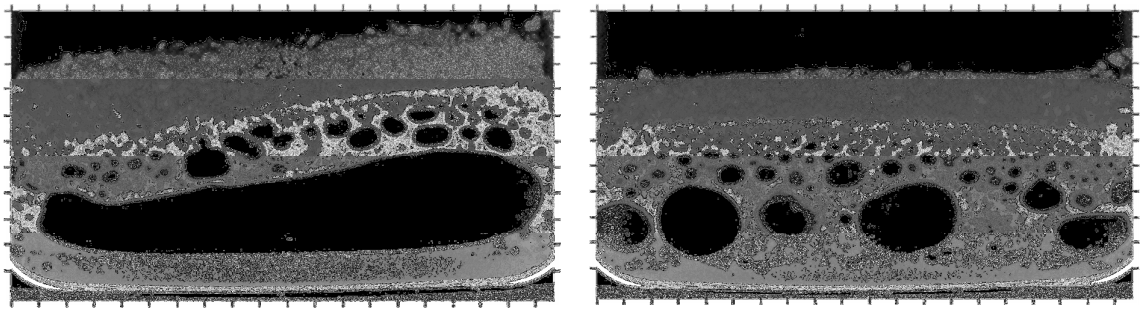

Fig. 17. X-ray tomography images of two different melter feeds heated from below [31]. The horizontal dimension of the platinum beaker is 10 cm. The heating time was 22 min. Bubbles coalesce into cavities that merge and become large when obstructed by crucible walls.

Fig. 18. Cross-section of HLW melter feed sample heated at 5°C min^{-1} to 800°C and quenched. The diameter of the bottom of the porcelain crucible is 22 mm. Note two large cavities in the sample. The foam was collapsing internally via coalescence of growing bubbles rather than via bursting of rising bubbles at the melt surface.

Regarding the motion of cavities, an alternative scenario is conceivable. One can assume that a cavity is growing from a single bubble via coalescence with bubbles of both primary and secondary foams and with other cavities until it grows to the proximity of a vent hole or the cold cap edge to which the gas is released. The cavity is annihilated and a new one begins to grow. The cavities do not move; they grow, coalesce, burst, and grow again. This periodic process can be treated via representative averaging of the cavity thickness and area coverage.

The top temperature of the cavity layer was estimated in this study as a maximum on the foaming curve. Although this assumption is strongly plausible owing to the rapid collapse of the feed after maximum expansion is reached, it may be modified based on future data.

5.2 Primary foaming

Generally, feeds exhibiting ample primary foaming, such as the A0 feed with Al_2O_3 as alumina source [23], melt at considerably slower rates than other feeds [21]. In this case, primary foam becomes the main resistance for the heat transfer to the cold cap. It is possible that this is due to ample primary foam collapsing at a slower rate, shifting T_C to a higher temperature.

Primary foam can be considerably decreased by a proper selection of source materials. The objective is to choose materials that keep porosity open until chemical reactions are complete or near completion (e.g. T_P is >800°C). In other words, primary foam can be minimized through releasing most if not all batch gases before the glass-forming melt becomes connected or delaying the development of a continuous glass-forming melt until the batch gases are fully released.

5.3 Secondary foam

Low-density foam has solid-like behavior [32]. Hence, secondary foam is unlikely to be dragged by the natural (buoyancy driven) flow of molten glass below the cold cap. This may explain why no foam is observed around the cold cap edges. However, convection forced by vigorous bubbling is strong enough to remove secondary foam.

5.4 Bubbling

As evident from experimental studies [33], bubbling has a tremendous effect on the melting rate. According to the recent report, the rate of melting was as high as 1400 kg m^{-2} day^{-1}. Such a high performance can be attributed to the following factors:

1) Bubbling generates forced convection in the molten glass that greatly exceeds natural convection driven by buoyancy. As a result, velocity gradients under the secondary foam layer become steeper, the thermal boundary layer is suppressed, and the T_B rises. However, as Fig. 6 shows, T_B increase alone cannot account for the increase of the rate of melting demonstrated in [33].
2) It is likely that large bubbles from bubblers sweep the secondary foam from beneath the cold cap and thus increase the transferred heat. The complete removal of secondary foam would be equivalent to zero foaminess.
3) Not only the large bubbles from bubblers sweep secondary foam from beneath the cold cap, they also bring the hot glass directly to the primary foam bottom. The increased temperature transfers more heat to the cold cap. This assumption is supported by the fact that distributed bubbling further increases the melting rate [33].
4) As bubblers bring hot gas to the plenum space, the temperature increases to ~600°C, thus increasing the fraction of heat flux to the cold cap from above.
5) Feed can be stirred into the melt by the vigorous flow of gas from the bubblers which form vent holes directly above bubblers, exposing a fraction of the feed to high temperatures at which batch reactions are rapid and gases are quickly released if the viscosity is low enough.

5.5 Incorporation of the cold cap model into the model of whole glass melter

The incorporation of the cold cap model into the model of the whole waste glass melter, such as that developed by Schill [34], is straightforward. The coupled boundary conditions are the top and bottom temperatures of the cold cap and the heat fluxes to the cold cap from below and from above. The coupled model will iteratively merge both models until a steady state is reached.

6. Conclusions

An advanced 1D model for the cold cap in a slurry-fed waste glass melter has been developed. The model solves simplified balances of mass and energy using the finite volume method and incorporates the structure and dynamics of three-layered foam that separates the reacting batch from molten glass. The existence of the three-layered structure appears to be supported by experimental data.

The model estimates the melting rate of glass batches as a function of batch properties and melter operating conditions, such as the conversion enthalpy of the feed, the temperature at the bottom of the cold cap, the fraction of heat flux to the cold cap from above, and the foaminess of the feed. Additional model outcomes include the distributions of temperature, velocity, and local heating rate, together with profiles of fractions of undissolved quartz particles and spinel crystals within the cold cap.

The model is suitable for situations where no or limited bubbling is introduced to the melter from bubblers. In the case of strong bubbling, the model would underestimate its effect on the melting rate. As strong bubbling is becoming a norm in a waste glass melting technology, future model improvements should focus on the incorporation of the effect of bubbling on the cold cap and foam behavior. Finally, the cold cap model will be incorporated in the model of the glass melter as its integral component.

Acknowledgements

This work was supported by the Department of Energy's Waste Treatment and Immobilization Plant Federal Project Office under the direction of Dr. Albert A. Kruger and by the WCU (World Class University) program through the National Research Foundation of Korea funded by the Ministry of Education, Science and Technology (R31 - 30005). Richard Pokorny acknowledges financial support from the specific university research (MSMT No 20/2013). The authors are grateful to Jaehun Chun and Dong-Sang Kim for insightful discussions, David A. Pierce for TGA and differential scanning calorimetry measurements, and Derek R. Dixon for providing cold cap images. Pacific Northwest National Laboratory is operated for the U.S. Department of Energy by Battelle under Contract DE-AC05-76RL01830.

References

1. R.A. Kirkbride, G.K. Allen, R.M. Orme, R.S. Wittman, J.H. Baldwin, T.W. Crawford, J. Jo, L.J. Fergestrom, T.M. Hohl, D.L. Penwell, Tank waste remediation system operation and utilization plan, Vol. I, HNF-SD-WM-SP-012, Numatec Hanford Corporation, Richland,Washington (1999).
2. Z. Feng, D. Li, G. Qin, S. Liu, J. Am. Ceram. Soc. 91 (2008) 3229–3234.
3. A. Abbassi, Kh. Khoshmanesh, Appl. Therm. Eng. 28 (2008) 450–459.
4. C.C. Yen, W.S. Hwang, Mater. Trans. 49 (2008) 766–773.
5. H. Mase, K. Oda, J. Non-Cryst. Solids 38–39 (1980) 807–812.
6. R. Viskanta, X. Wu, J. Am. Ceram. Soc. 67 (1984) 376–380.
7. A. Ungan, R. Viskanta, AIChE Sym. S., No. 236, Vol. 80 (1984) 446–451.
8. P. Hrma, Glastech. Ber. 55 (1982) 138–150.
9. P. Schill, Ceram.-Silik. 26 (1982) 155–163.
10. P. Schill, Ceram.-Silik. 26 (1982) 209–222.
11. P. Hrma, A.A. Kruger, R. Pokorny, J. Non-Cryst. Solids 358 (2012) 3559–3562.
12. R. Pokorny, P. Hrma, J. Nucl. Mater. 429 (2012) 245–256.
13. R. Pokorny, J.A. Rice, J.V. Crum, M.J. Schweiger, P. Hrma, J. Nucl. Mater., 443 (2013) 230–235.
14. J. Chun, D.A. Pierce, R. Pokorný, P. Hrma, Thermochim. Acta 559 (2013) 32–39.
15. R. Pokorny, J.A. Rice, M.J. Schweiger, P. Hrma, J. Am. Ceram. Soc. 96 (2013) 1891–1898.
16. M. Iguchi, J.O. Ilegbusi, Modeling multiphase materials processes: Gas-liquid systems, Springer, New York, (2010).
17. P. Hrma, J. Colloid Interf. Sci. 134 (1990) 161–168.
18. J. J. Bikerman, Physical Surfaces, Academic Press, New York/London, 1970, p. 150; see also Trans. Faraday Soc. 34 (1948) 634-638.
19. P. Hrma, M.J. Schweiger, C.J. Humrickhouse, J.A. Moody, R.M. Tate, T.T. Rainsdon, N.E. TeGrotenhuis, B.M. Arrigoni, J. Marcial, C.P. Rodriguez, B.H. Tincher, Ceram.-Silik. 54 (2010) 193–211.
20. M.J. Schweiger, P. Hrma, C.J. Humrickhouse, J. Marcial, B.J. Riley, N.E. TeGrotenhuis, J. Non-Cryst. Solids 356 (2010) 1359–1367.
21. K.S. Matlack, W. Kot, W. Gong and I.L. Pegg, Small scale melter testing of HLW algorithm glasses: matrix 1 tests, VSL-07R1220-1, Vitreous State Laboratory of the Catholic University of America, 2007.
22. S.H. Henager, P. Hrma, K.J. Swearingen, M.J. Schweiger, J. Marcial, N.E. TeGrotenhuis, J. Non-Cryst. Solids 357 (2011) 829–835.
23. D.A. Pierce, P. Hrma, J. Marcial, B.J. Riley, M.J. Schweiger, Int. J. Appl. Glass Sci. 3 (2012) 59–68.
24. R. Pokorny, D.A. Pierce and P. Hrma, Thermochim. Acta 541 (2012) 8–14.

25. P. Schill, Modeling the behavior of noble metals during HLW vitrification, in: W. Lutze, Modeling the behavior of noble metals during HLW vitrification in the DM1200 melter, VSL-05R5740-1, Vitreous State Laboratory, Washington DC (2005).
26. J. Matyas, J. D. Vienna, A. Kimura, M. J. Schaible, R. M. Tate, Chapter 5 in: K. Fox, E. Hoffman, N. Manjooran, G. Pickrell (Eds.), Development of Crystal-Tolerant Waste Glasses, Advances in Materials Science for Environmental and Nuclear Technology: Ceramic Transactions, 222, John Wiley & Sons, Inc., Hoboken, NJ, 2010, pp. 41–51.
27. R. Conradt: The industrial glass melting process. In: The SGTE casebook – Thermodynamics at work, K. Hack, (Ed.), CRC Press, Boca Raton 2008, Chapter II.24, 282–303.
28. K.S. Matlack, H. Gan, M. Chaudhuri, W. Kot, W. Gong, T. Bardakci, I.L. Pegg, J. Innocent, DM100 and DM1200 melter testing with high waste loading glass formulations for Hanford high-aluminum HLW streams, VSL-10R1690-1, Vitreous State Laboratory, The Catholic University of America, Washington, DC (2010).
29. D.S. Kim, M.J. Schweiger, W.C. Buchmiller, J. Matyas, Laboratory-scale melter for determination of melting rate of waste glass feeds. PNNL-21005; EMSP-RPT-012, Pacific Northwest National Laboratory, Richland, Washington, (2012).
30. D.R. Dixon, M.J. Schweiger, P. Hrma, Effect of feeding rate on the cold cap configuration in a laboratory-scale melter, WM2013 Conference, February 24–28, 2013, Phoenix, Arizona USA.
31. A.S. Choi, D.H. Miller, D.M. Immel, Determination of HLW glass melt rate using X-ray computed tomography (CT), SRNL-STI-2010-00767, Rev. 0, Savannah River National Laboratory, Aiken, South Carolina (2010).
32. N.D. Denkov, S.S. Tcholakova, R. Höhler, S. Cohen-Addad, Foam Rheology, in: Foam Engineering: Fundamentals and Applications, P. Stevenson (Ed.), John Wiley & Sons, Ltd, Chichester, UK, 2012, 91–120, Chapter 6.
33. K.S. Matlack, W.K. Kot, R.A. Callow, J. Innocent, I.L. Pegg, Testing of optimized bubbler configuration for HLW Melter, VSL-13R2950-1, Vitreous State Laboratory, The Catholic University of America, Washington, DC (2013).
34. P. Schill, W. Lutze, W. Gong, I.L. Pegg, Glass Technol.-Part A 48 (2007) 276–289.